



# HAWC+/SOFIA Polarimetry in L1688: Relative Orientation of Magnetic Field and Elongated Cloud Structure

Dennis Lee<sup>1,2</sup>, Marc Berthoud<sup>1,3</sup>, Che-Yu Chen<sup>4,5</sup>, Erin G. Cox<sup>1</sup>, Jacqueline A. Davidson<sup>6</sup>, Frankie J. Encalada<sup>7</sup>, Laura M. Fissel<sup>8</sup>, Rachel Harrison<sup>7</sup>, Woojin Kwon<sup>9,10</sup>, Di Li<sup>11,12</sup>, Zhi-Yun Li<sup>4</sup>, Leslie W. Looney<sup>7</sup>, Giles Novak<sup>1,2</sup>, Sarah Sadavoy<sup>8</sup>, Fabio P. Santos<sup>13</sup>, Dominique Segura-Cox<sup>14</sup>, and Ian Stephens<sup>15</sup>

<sup>1</sup> Center for Interdisciplinary Exploration and Research in Astrophysics (CIERA), 1800 Sherman Avenue, Evanston, IL 60201, USA

<sup>2</sup> Department of Physics & Astronomy, Northwestern University, 2145 Sheridan Road, Evanston, IL 60208, USA

<sup>3</sup> Engineering + Technical Support Group, University of Chicago, Chicago, IL 60637, USA

<sup>4</sup> Department of Astronomy, University of Virginia, Charlottesville, VA 22904, USA

<sup>5</sup> Lawrence Livermore National Laboratory, Livermore, CA 94550, USA

<sup>6</sup> University of Western Australia, School of Physics, 35 Stirling Highway, Crawley, WA 6009, Australia

<sup>7</sup> Department of Astronomy, University of Illinois, 1002 West Green Street, Urbana, IL 61801, USA

<sup>8</sup> Department of Physics, Engineering and Astronomy, Queen's University, 64 Bader Lane, Kingston, ON K7L 3N6, Canada

<sup>9</sup> Department of Earth Science Education, Seoul National University, 1 Gwanak-ro, Gwanak-gu, Seoul 08826, Republic of Korea

<sup>10</sup> SNU Astronomy Research Center, Seoul National University, 1 Gwanak-ro, Gwanak-gu, Seoul 08826, Republic of Korea

<sup>11</sup> CAS Key Laboratory of FAST, National Astronomical Observatories, Chinese Academy of Sciences, Beijing 100101, People's Republic of China

<sup>12</sup> University of Chinese Academy of Sciences, Beijing 100049, People's Republic of China

<sup>13</sup> Max Planck Institute for Astronomy, Königstuhl 17, D-69117 Heidelberg, Germany

<sup>14</sup> Center for Astrochemical Studies, Max Planck Institute for Extraterrestrial Physics, D-85748 Garching, Germany

<sup>15</sup> Department of Earth, Environment and Physics, Worcester State University, Worcester, MA 01602, USA

Received 2020 November 20; revised 2021 June 14; accepted 2021 June 17; published 2021 September 3

## Abstract

We present a study of the relative orientation between the magnetic field and elongated cloud structures for the  $\rho$  Oph A and  $\rho$  Oph E regions in L1688 in the Ophiuchus molecular cloud. Combining inferred magnetic field orientation from HAWC+ 154  $\mu$ m observations of polarized thermal emission with column density maps created using Herschel submillimeter observations, we find consistent perpendicular relative alignment at scales of 0.02 pc (33'' at  $d \approx 137$  pc) using the histogram of relative orientations (HRO) technique. This supports the conclusions of previous work using Planck polarimetry and extends the results to higher column densities. Combining this HAWC+ HRO analysis with a new Planck HRO analysis of L1688, the transition from parallel to perpendicular alignment in L1688 is observed to occur at a molecular hydrogen column density of approximately  $10^{21.7} \text{ cm}^{-2}$ . This value for the alignment transition column density agrees well with values found for nearby clouds via previous studies using only Planck observations. Using existing turbulent, magnetohydrodynamic simulations of molecular clouds formed by colliding flows as a model for L1688, we conclude that the molecular hydrogen volume density associated with this transition is approximately  $\sim 10^4 \text{ cm}^{-3}$ . We discuss the limitations of our analysis, including incomplete sampling of the dense regions in L1688 by HAWC+.

*Unified Astronomy Thesaurus concepts:* Star formation (1569); Interstellar medium (847); Interstellar magnetic fields (845); Molecular clouds (1072); Giant molecular clouds (653)

## 1. Introduction

The interstellar magnetic field is believed to play important roles in star formation. For example, the field is thought to be one of the key factors—along with gravity and turbulence—that determines and regulates the rate at which the molecular cloud evolves to form clumps, filaments, cores, and, finally, newborn stars (McKee & Ostriker 2007). On smaller scales, the field may also strongly influence the formation of protoplanetary disks (Li et al. 2014).

A common method for observing magnetic fields in molecular clouds is measuring the linearly polarized thermal radiation emitted by dust grains within these clouds (Hildebrand et al. 2000). While the exact physical process by which these grains are aligned remains an open question, they are generally understood to orient themselves with the long axes perpendicular to the orientation of the local magnetic field lines (Andersson et al. 2015). As a result, the far-infrared to submillimeter thermal emission is linearly polarized perpendicular to the magnetic field, thus indirectly tracing the projection of the field on the sky.

An effective method for using these polarization measurements to understand the magnetic field's role is to compare the inferred orientation and morphology of the magnetic field to the orientations of elongated molecular cloud structures (e.g., Tassis et al. 2009; Sugitani et al. 2011; Li et al. 2013; Palmeirim et al. 2013; Soler et al. 2013; Matthews et al. 2014; Planck Collaboration et al. 2016a, 2016b). Soler et al. (2013) introduced a statistical technique to do so known as the histogram of relative orientations (HRO) method. When applied to synthetic polarization measurements from magnetohydrodynamic (MHD) simulations, it was found that the gas structures in column density maps showed preferential alignment with magnetic field orientations depending on physical conditions. At low column densities, gas structures showed preferred parallel alignment. With sufficiently high magnetization, this preference changes from parallel to perpendicular at higher column densities. Notably, Soler et al. (2013) showed that super-Alfvénic models do not predict a transition to perpendicular alignment at any column densities below  $N_{\text{H}_2} \approx 10^{22.5} \text{ cm}^{-2}$  ( $N_{\text{H}} \approx 10^{22.8} \text{ cm}^{-2}$ ).

Subsequent theoretical work continued to investigate the nature of the relative orientation relationship between the magnetic field and column density structure (e.g., Chen et al. 2016; Soler & Hennebelle 2017; Körtgen & Soler 2020; Seifried et al. 2020). It has been suggested that HROs can be used as a tool to estimate both the volume density and the magnetic field strength at the transition (Chen et al. 2016). Recent HRO analyses of numerical simulations confirmed that the transition is only clearly evident in simulations with high magnetization and that the transition density threshold is primarily dependent on the magnetization of the gas (e.g., Soler & Hennebelle 2017; Körtgen & Soler 2020). Seifried et al. (2020) found that projection effects may prevent the observation of a transition, even when one exists.

Application of the HRO analysis to actual molecular clouds requires a large number of polarization measurements. In Planck Collaboration et al. (2016b), this method was applied to 10 molecular clouds using  $10'$  resolution Planck polarization maps at 353 GHz. Most clouds (eight of 10) exhibited a transition from parallel to perpendicular alignment, with an average transition column density of  $N_{\text{H}_2} \approx 10^{21.4} \text{ cm}^{-2}$  ( $N_{\text{H}} \approx 10^{21.7} \text{ cm}^{-2}$ ). This result implies that most of the sampled clouds possess at least a moderately strong magnetic field (i.e., the clouds are either trans- or sub-Alfvénic). Soler et al. (2017) applied the HRO method to submillimeter polarization measurements of Vela C from the BLASTPol balloon-borne polarimeter (Fissel et al. 2016). A similar result was found.

However, the  $10'$  ( $\sim 0.5$  pc for clouds at  $d \sim 137$  pc) Planck resolution can only probe the cloud-scale polarization, while the magnetic field structure at subparsec scales and higher column densities could have a more direct impact on the star-forming process. On the other hand, the Atacama Large Millimeter/submillimeter Array is capable of high-sensitivity polarization measurements of cores and envelopes but is unable to map larger scales. Mounted on the Stratospheric Observatory for Infrared Astronomy (SOFIA), the HAWC+ far-infrared polarimeter (Harper et al. 2018) provides the ability to produce higher-resolution maps coupled with a large detector area at these intermediate scales (e.g., Chuss et al. 2019; Santos et al. 2019). This allows us to further extend analyses done with the HRO technique.

Here we apply the HRO method to polarimetric observations of the L1688 region in the Ophiuchus molecular cloud. At a distance of approximately 137 pc, Ophiuchus is one of the closest star-forming clouds (Wilking et al. 2008; Zucker et al. 2019). In order to investigate a range of column densities, we use Planck polarization measurements for the low column densities and HAWC+ observations of the  $\rho$  Oph A and  $\rho$  Oph E regions within L1688 for the high column densities. Studies of L1688 have revealed a large and varied population of protostars, making it an attractive target for studying low-mass star formation (Motte et al. 1998; Enoch et al. 2009; Sadavoy et al. 2019).

The paper is organized as follows. Section 2 describes our HAWC+ observations and presents Herschel column density maps and Planck Stokes parameter measurements of L1688. Section 3 summarizes the HRO method and its application here to the HAWC+ and Planck data. In Section 4, we present our main results. Section 5 discusses the results and their implications. Finally, Section 6 provides a summary.

## 2. Observations

### 2.1. HAWC+/SOFIA Observations

Observations of  $\rho$  Oph A and  $\rho$  Oph E were made using the HAWC+ polarimeter mounted on SOFIA. Both sources were observed in Band D ( $154 \mu\text{m}$ ), providing an FWHM resolution of  $13''.6$ . As part of the HAWC+ Guaranteed Time Observing (GTO) program,  $\rho$  Oph A was observed in 2017 May.  $\rho$  Oph E was observed on 2018 July 7 (AOR: 06\_0116\_6).

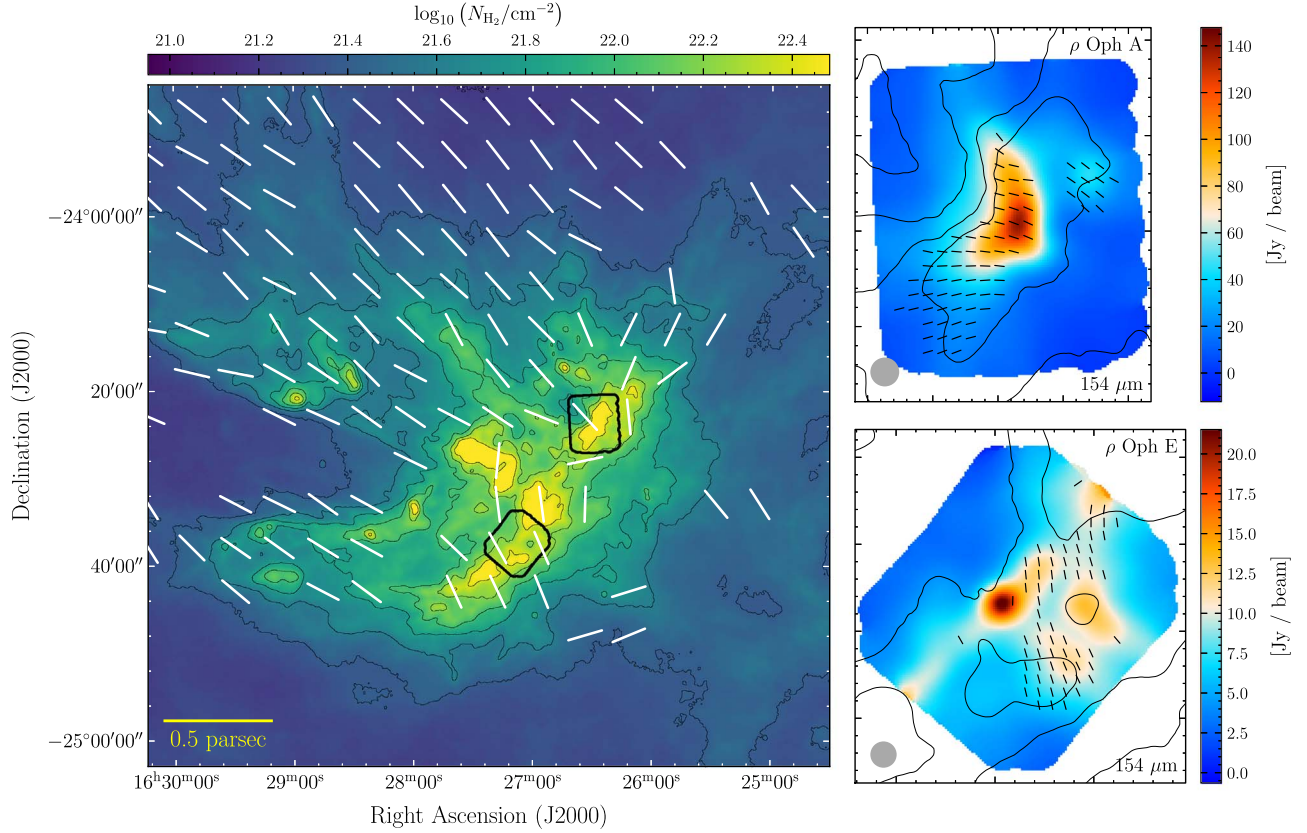
Observations of  $\rho$  Oph E were made in the matched–nod–chop mode with a chopping frequency of 10.2 Hz and a chop throw of  $430''$ . Measuring from equatorial north and increasing toward the east, we used a chop angle of  $60^\circ$ . The observations of  $\rho$  Oph E totaled 746 s on source. The observations were divided into seven “dither sets,” with each set consisting of four independent pointings. The dither offset between each independent pointing was  $40''$ , with each independent pointing containing observations at four different half-wave plate angles.

Observations of  $\rho$  Oph A were also made in the matched–nod–chop mode and totaled 833 s. Further details on the observations of  $\rho$  Oph A can be found in Santos et al. (2019), where the data were first presented and discussed. The regions of  $\rho$  Oph A and  $\rho$  Oph E observed are indicated on the Herschel-derived column density map of L1688 by solid black outlines in Figure 1 (André et al. 2010; Ladjelate et al. 2020).

The observations for both regions were manually reduced using the HAWC+ Data Reduction Pipeline following the procedure described by Santos et al. (2019). The process is briefly summarized here.

The raw time-ordered data are first demodulated to account for the chopping. During this process, we also discard data affected by erroneous telescope movement or other data acquisition errors. Flat-fielding is then done to calibrate for any pixel-to-pixel gain variations. Data from dead or noisy pixels are then removed. Next, the demodulated time-ordered data are combined into four sky images per independent pointing, i.e., one image per half-wave plate position. These four images are then summed and differenced to obtain final Stokes  $I$ ,  $Q$ , and  $U$  maps for each independent pointing. After flux calibrations and corrections for atmospheric opacity are completed, the results from each independent pointing are combined to create final Stokes  $I$ ,  $Q$ , and  $U$  maps. The final polarization percentage is also computed and debiased. For the total flux calibration, we estimate an absolute uncertainty of 20%. The  $\chi^2$  statistic is then computed for the entire data set in order to evaluate the consistency between each repeated measurement. The purpose is to test for additional sources of uncertainties (Davidson et al. 2011; Chapman et al. 2013). The typical cause of these additional uncertainties is noise that is correlated across instrument pixels. The final reported uncertainties in Stokes  $I$ ,  $Q$ , and  $U$  are then inflated to adjust for the underestimation.

Next, we reject polarization measurements based on several different criteria. Measurements possessing a degree of polarization less than three times the corresponding polarization uncertainty ( $p < 3\sigma_p$ ) or a polarization angle uncertainty greater than  $10^\circ$  are rejected. Nonphysical measurements of polarization ( $p > 50\%$ ) are also rejected. The cause of these high  $p$  values is not known, but less than 0.5% of the data were removed as a result of this cut. Any polarization measurement with a corresponding total intensity of less than 1% of the



**Figure 1.** Left: Herschel column density map of L1688 shown in contours and color map. Black outlines indicate the regions of  $\rho$  Oph A and  $\rho$  Oph E observed using HAWC+. White line segments represent the native resolution inferred magnetic field orientation as observed by Planck at 353 GHz (Section 2.2). Line segments are shown where  $P/\sigma_P > 3$ , with spacing corresponding to the Planck beam size ( $\sim 5'$ ), and are drawn with uniform length. A scale bar is shown at the lower left of the panel. Right: HAWC+ 154  $\mu\text{m}$  total intensity shown as a color map for  $\rho$  Oph A (top) and  $\rho$  Oph E (bottom) smoothed to  $36''/3$  resolution to match the Herschel column density resolution of our HRO analysis (see Sections 2.3 and 3.1). The magnetic field orientation, also at  $36''/3$  resolution, is indicated by the Nyquist-sampled uniform-length black line segments. These are limited to measurements meeting the criteria described in Section 2.1 (e.g.,  $p/\sigma_p > 3$ ). The beam is depicted in the lower left corner. For reference, the Herschel column density is indicated by the black contours. Contour levels for all Herschel maps are in units of  $\log_{10}(N_{\text{H}_2} \text{ cm}^{-2})$ , with the highest contour at 22.4 and decreasing in steps of 0.2.

measured peak ( $I < 0.01 \text{ peak}(I)$ ) or a total intensity uncertainty greater than 10% of the total intensity (i.e.,  $S/N < 10$ ) was excluded.

Since both  $\rho$  Oph A and  $\rho$  Oph E were observed in the matched-nod-chop mode, we also consider contamination from polarization in the reference beam areas. To do so, we flag sky positions where the differenced polarized flux is less than the average polarized flux for the two corresponding reference beam locations. This method is based on the analysis described in Novak et al. (1997) and Chuss et al. (2019). For each sky pixel, where  $p_m$  is the measured polarization fraction and  $p_r$  is the polarization in the reference beam, we reject pixels where

$$p_m^2 < (p_r w)^2. \quad (1)$$

Here  $w$  is the expected ratio of reference beam intensity to differenced intensity,

$$w = \left( \frac{\bar{I}_r}{I_s - \bar{I}_r} \right), \quad (2)$$

where  $I_s$  is the intensity in the source region. Herschel 160  $\mu\text{m}$  intensity maps of the region are used to estimate  $w$ . As each source was observed with two reference beam areas, symmetrically located on either side of the central area,  $\bar{I}_r$  represents the average of the intensities in these two areas. We use a

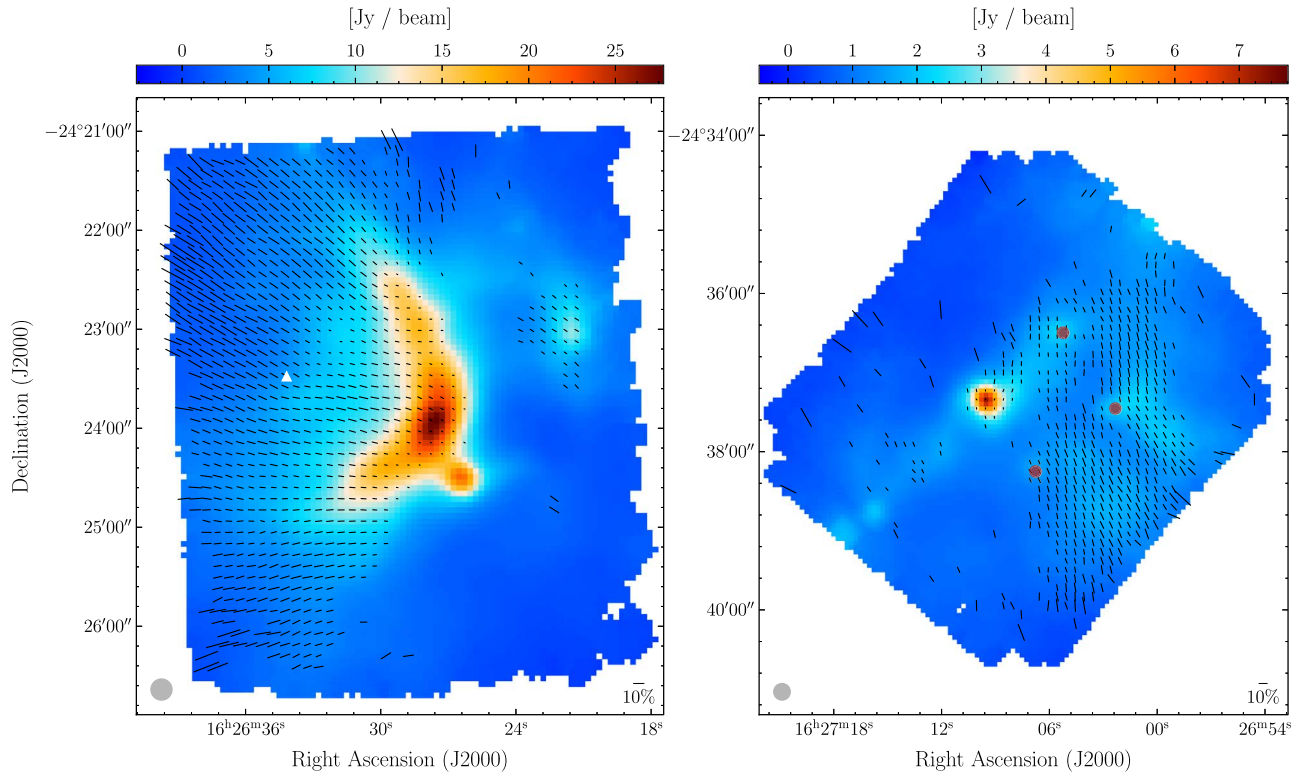
conservative estimate where the reference beam area has a uniform polarization of  $p_r = 0.1$ .

Any pixels that are flagged by the condition described in Equation (1) are discarded, as they are considered too contaminated to be of use. For measurements that survive, there nonetheless remains the possibility of some contamination, even if to a lesser degree. A more detailed analysis designed to more carefully quantify the impact of the reference beam—specifically on the measured polarization angle and its effect on subsequent analyses—can be found in Section 5.2 and Appendix.

The resulting HAWC+ observations of  $\rho$  Oph A and  $\rho$  Oph E are shown in Figure 2, where the magnetic field orientation is inferred by rotating the polarization measurements by  $90^\circ$ .

Comparing the resulting reduction of  $\rho$  Oph A presented here with the one presented in Santos et al. (2019), the basic morphology of the magnetic field is generally the same. However, owing to the different approaches used to consider the reference beam effects, there are small variations in the spatial coverage of the polarization measurements. Beyond this, we note several other minor differences. First, the pointing is verified based on comparison with the Herschel PACS 160  $\mu\text{m}$  maps of Ophiuchus obtained from the Herschel Science Archive (Poglitsch et al. 2010) and thus differs slightly





**Figure 2.** The HAWC+ 154  $\mu\text{m}$  total intensity maps and inferred magnetic field orientation for  $\rho$  Oph A (left) and  $\rho$  Oph E (right). The inferred field orientation is indicated by the Nyquist-sampled black line segments. These line segments are scaled based on the polarization percentage (note the 10% scale bar in the lower right of each map) and limited to measurements meeting the criteria described in Section 2.1 (e.g.,  $p/\sigma_p > 3$ ). In the left panel, the white triangle marks the location of Oph S1 (Andre et al. 1988; Hamaguchi et al. 2003). In the right panel, the red circles indicate the locations of three protostars. These are in addition to Elias 29, a class I protostar located at the source peak. Clockwise from the source peak, the three protostars are LFAM 26, WL 16, and WL 17, all believed to be class I protostars (Enoch et al. 2009). The beam size of  $13''.6$  is shown in the lower left of each panel.

between the two results. Additionally, the  $\chi^2$  analysis finds an underestimation of the uncertainties by approximately 36% versus 38% in Santos et al. (2019).

### 2.2. Planck Stokes Parameter Maps

In order to investigate the low column density regions of L1688, we use all-sky linear polarization measurements from Planck. At 353 GHz, these measurements have a native resolution of  $5'$ . We use Stokes  $Q$  and  $U$  maps from Data Release 3, available on the Planck Legacy Archive (Collaboration et al. 2020). The tangent plane projection is produced for the L1688 region, defined by a  $1.3^\circ \times 1.3^\circ$  region (see Figure 1). To remove low-quality measurements, polarization measurements possessing a polarized intensity less than three times the corresponding polarized intensity uncertainty ( $P < 3\sigma_P$ ) are rejected. The resulting inferred magnetic field orientations are plotted in Figure 1. Compared to the smoothed  $10'$  resolution, 353 GHz Planck inferred magnetic field used in Planck Collaboration et al. (2016b), these higher-resolution data are largely consistent.

### 2.3. Herschel Column Density Maps

A column density map for L1688 was obtained from the publicly available Herschel Gould Belt Survey Archive (André et al. 2010). The 160, 250, 350, and 500  $\mu\text{m}$  Herschel observations of Ophiuchus were fit to a modified blackbody function in order to produce Herschel column density maps at a resolution of  $36''.3$  (see Ladjelate et al. 2020 for more details). The column density map is shown in Figure 1. In addition to

the  $36''.3$  resolution column density map, a “high-resolution” column density map with an effective resolution of  $18''.2$  created through a multiscale decomposition method is also available (Palmeirim et al. 2013). However, to be conservative, we have opted to use the native  $36''.3$  resolution column density map.

## 3. Histogram of Relative Orientations

In Figure 1, we see that the inferred magnetic field orientation is preserved across the Planck and HAWC+ measurements despite the factor of nine difference in angular resolution. This continuity has motivated us to conduct a joint HAWC+/Planck HRO analysis of L1688. The HRO method is designed to characterize the orientation of the magnetic field in the context of column density structures (Soler et al. 2013; Planck Collaboration et al. 2016b; Hull et al. 2017; Fissel et al. 2019). In particular, this method describes any preference for parallel or perpendicular alignment of the magnetic field with respect to elongated structures seen in column density maps. In the present paper, we apply this method to both the HAWC+ and Planck data sets described in Section 2. The procedure for each case is nearly identical. Differences are highlighted in the description of the analysis below.

### 3.1. HRO Construction

The relative orientation between the density structure and the magnetic field as projected onto the plane of the sky can be characterized by the angle  $\phi$ , defined as the relative angle between the projected magnetic field vector  $\hat{B}$  and the line

tangent to the local isocontour of gas column density (note that this is as applied to observations in 2D; Section 5.3 will discuss the analogous application in 3D). Equivalently, this can be defined as the relative orientation angle between the polarization vector ( $\hat{E}$ ) and the gradient of the column density structure ( $\nabla N$ ). The HRO is the distribution of the relative orientations  $\phi$ .

For consistency, prior to the HAWC+ HRO analysis, we smooth the 13''6 resolution HAWC+ Stokes  $Q$  and  $U$  observations to the 36''3 resolution of the Herschel column density maps. Smoothed HAWC+ polarimetry results are shown in Figure 1. Similarly, for the Planck analysis, we smooth the 36''3 resolution Herschel column density maps to the 5' resolution of the Planck data.

For the HAWC+ analyses, following the IAU convention, the angle of  $\hat{E}$  is computed from the  $Q$  and  $U$  values by

$$\psi_{\hat{E}} = \frac{1}{2} \arctan(U, Q). \quad (3)$$

Due to the different conventions followed by the Planck Stokes parameters, the following is used for Planck data:

$$\psi_{\hat{E}} = \frac{1}{2} \arctan(-U_{\text{Planck}}, Q_{\text{Planck}}). \quad (4)$$

Details can be found in Section 2.1 of Planck Collaboration et al. (2015).

All data are then regridded onto a 3'' pixel size grid. We use a Gaussian derivative kernel to calculate the gradient ( $\nabla N$ ). For the column density maps to be compared with the HAWC+ polarization angle, we chose a kernel with an FWHM of 12''. For the column density maps to be compared with the Planck polarization angle, we chose a kernel with an FWHM of 30''. These kernel sizes are chosen such that they are large enough to smooth out and remove any potential edge or corner effects that may create erroneous gradient vectors, yet small enough such that no significant degradation of the resolution of our gradient map occurs.

Using both the polarization vector and the gradient vector, the relative orientation angle ( $\phi$ ) is then computed using

$$\phi = \arctan(|\nabla N \times \hat{E}|, \nabla N \cdot \hat{E}). \quad (5)$$

Under this convention,  $\phi = 0^\circ$  represents parallelism between the magnetic field and elongated column density structures, while  $\phi = \pm 90^\circ$  represents perpendicularity between the magnetic field and elongated column density structures.

Next, for both the Planck and HAWC+  $\phi$  maps separately, the respective map is divided into four bins that are ordered by  $N_{\text{H}_2}$ . The column density ranges for the four bins are determined by constraining each bin to have the same number of data points. For each of these four bins, an HRO is then produced. This results in a total of eight HRO analyses, four for Planck and four for HAWC+.

Due to the fact that the HAWC+ observations cover only  $\rho$  Oph A and  $\rho$  Oph E, they sample only a minor portion of the high column density sight lines in L1688. On the other hand, the Planck maps cover the majority of the low column density sky area in the region studied. Accordingly, we make a cut on the column density for the HAWC+ data to remove column densities satisfying  $\log_{10}(N_{\text{H}_2}) < 22.3$ . At column densities lower than this threshold, the HAWC+ observations only sample  $\sim 1\%$  of the available sky area in L1688, whereas for column densities above this threshold, the undersampling is not

as severe. The effects of this ‘‘sampling uncertainty’’ on our conclusions are discussed in Sections 5.2 and 5.3. Note that the column density cut is applied before the HAWC+ data are divided into four column density bins (see previous paragraph).

### 3.2. Relative Orientation Parameter

The characteristic shape of the histogram describing the distribution of  $\phi$  can be represented using  $\xi$ , the normalized version of the HRO shape parameter (Soler et al. 2013; Planck Collaboration et al. 2016a). The parameter is defined as

$$\xi = \frac{A_c - A_e}{A_c + A_e}, \quad (6)$$

where  $\xi$  compares the area of the center of the histogram ( $A_c$ ) with the area of the extremes of the histogram ( $A_e$ ). The central area ( $A_c$ ) is defined as the area of the region:  $-22.5^\circ < \phi < 22.5^\circ$ . The extremes area ( $A_e$ ) is defined as the union of the two regions:  $-90^\circ < \phi < -67.5^\circ$  and  $67.5^\circ < \phi < 90^\circ$ .

Using this definition, we can see that  $\xi$  holds a value between  $-1$  and  $1$ . Here  $\xi > 0$  indicates a histogram with a peak between  $-22.5^\circ$  and  $22.5^\circ$ . This corresponds to a preference for parallel alignment between the elongation of the gas structure and the magnetic field. Conversely, when  $\xi < 0$ , this indicates a histogram where the magnetic field is largely perpendicular to the column density contours. In a situation of no alignment preference, the corresponding histogram will be largely flat, and the shape parameter will be approximately zero ( $\xi \approx 0$ ).

The uncertainty in  $\xi$  is  $\sigma_\xi$ , defined as

$$\sigma_\xi^2 = \frac{4(A_e^2 \sigma_{A_c}^2 + A_c^2 \sigma_{A_e}^2)}{(A_c + A_e)^4}, \quad (7)$$

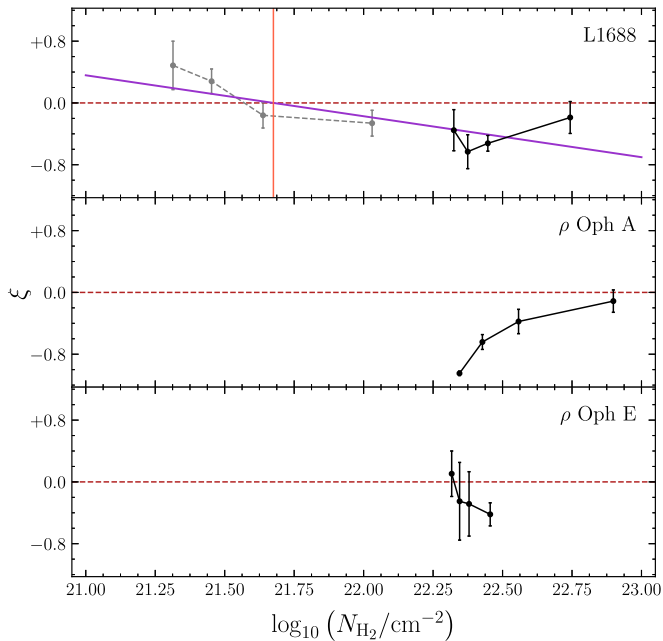
where  $\sigma_{A_c}^2$  and  $\sigma_{A_e}^2$  are the variances of  $A_c$  and  $A_e$ . As explained in Planck Collaboration et al. (2016b), this uncertainty represents the ‘‘jitter’’ of the histogram.

The HRO shape parameter ( $\xi$ ) is computed for each of the four bins consisting of Planck data and also for each of the four bins consisting of HAWC+ data. We then plot  $\xi$  as a function of column density bin (specifically of the median density value for the bin). This is shown in the top panel of Figure 3. Also shown separately in Figure 3 are the HAWC+ HRO results for  $\rho$  Oph A and  $\rho$  Oph E (lower panels).

## 4. Results

From Figure 3, we see that for all three calculations of the  $\xi$  values from HAWC+ (L1688,  $\rho$  Oph A, and  $\rho$  Oph E), we obtain predominantly negative values indicative of perpendicular alignment (black points). As discussed in Section 1, the HRO analysis in Planck Collaboration et al. (2016b) noted a transition from parallel alignment at low to perpendicular alignment at high column densities (i.e., from positive  $\xi$  to negative  $\xi$ ) in molecular clouds. This transition, as observed by Planck in L1688, can be seen in the gray points of Figure 3.

Viewing the combined Planck/HAWC+ result presented here as an extension of the Planck Collaboration et al. (2016b) analysis, we find evidence that the trend initially observed in Planck Collaboration et al. (2016b) continues smoothly to higher column density regimes, at least for L1688 (see Section 5.2).



**Figure 3.** The HRO shape parameter as a function of column density for L1688 (top),  $\rho$  Oph A (middle), and  $\rho$  Oph E (bottom). Solid black and dashed gray lines indicate HAWC+ and Planck data, respectively. All error bars indicate  $1\sigma$  uncertainties. In the top panel, the resulting least-squares fit of the merged Planck and HAWC+ data is shown in purple. The estimated transition column density ( $10^{21.7} \text{ cm}^{-2}$ ) is indicated by the vertical red line.

## 5. Discussion

### 5.1. Alignment of Magnetic Field and Elongated Cloud Structures

The parallel versus perpendicular magnetic field behavior has been theoretically predicted in models of star formation (Soler et al. 2013; André et al. 2014). In the model envisioned by André et al. (2014), filamentary structures play a major role in the star formation process. These molecular filaments are elongated structures that may be produced via mechanisms such as converging flows. They appear to accumulate mass via relatively lower-density “striations” running perpendicular to the axis of the relatively higher-density filament. In this picture, these low-density striations are expected to be parallel to the field lines. In turn, the field lines are thus perpendicular to the major axis of the higher-density filament. This would result in the low-density/parallel to high-density/perpendicular behavior that is consistent with what we observe in L1688 (see Figure 3).

This behavior is also supported by a number of prior observational studies. As discussed in Section 1, Planck Collaboration et al. (2016b) observed a transition from parallel to perpendicular alignment with increasing column density in 10 giant molecular clouds. This was also observed in Vela C (Soler et al. 2017). Soler (2019) combined observations of large-scale (Planck) magnetic field and small-scale (Herschel) column density to understand the orientation between column density structures and the magnetic field. While distinctly different from what is done here, their study also noted a trend of column density versus magnetic field relative orientation changing from preferentially parallel to perpendicular with increasing column density. Recent improvements in polarimetric instrumentation on the James Clerk Maxwell Telescope (JCMT) have enabled magnetic field observations at smaller

scales and higher column densities than are accessible via Planck data (Ward-Thompson et al. 2017). Though not using the HRO method, recent studies using the JCMT (e.g., Ward-Thompson et al. 2017; Liu et al. 2018; Soam et al. 2019; Doi et al. 2020; Pattle et al. 2021) have generally observed perpendicular alignment at these smaller scales.

Observations of Serpens South using HAWC+, as well as archival near-infrared data, also noted a general perpendicular behavior between the magnetic field and elongated structures (Pillai et al. 2020). However, one of the filaments exhibited a transition from perpendicular back to parallel alignment at higher column densities ( $N_{\text{H}_2} \approx 10^{22.3} \text{ cm}^{-2}$ ), suggesting that magnetic alignment behavior may be more complex. This return to parallel alignment is hinted at when examining our analysis of  $\rho$  Oph A in Figure 3. Given the uncertainties, however, observation of this putative new transition in  $\rho$  Oph A is tentative.

### 5.2. Estimating the Transition Column Density

As can be seen in Figure 3, our joint analysis of L1688 spans a sufficiently large range of column densities to include both the low-density/parallel and high-density/perpendicular regimes. By fitting the simple linear trend line described in Planck Collaboration et al. (2016b) and Soler et al. (2017), we can estimate a value for the transition column density. Using the Levenberg–Marquardt least-squares optimization algorithm as implemented in the Python `scipy` library, we find  $N_{\text{H}_{2,\text{tr}}} \approx 10^{21.7} \text{ cm}^{-2}$ . The result of the fit is shown in Figure 3. The statistical uncertainty from the fit is a factor of  $\approx 1.25$ . Note that this uncertainty is obtained by accounting for the “jitter” of the histogram ( $\sigma_\xi$ ; indicated in Figure 3 by the error bars). Note also that prior to fitting the data, we set the uncertainty for a given value of  $\xi$  equal to the greater of (a) its corresponding uncertainty  $\sigma_\xi$  and (b) the median value of  $\sigma_\xi$  for all data points from the corresponding instrument (Planck or HAWC+) used in the fit. The reason for this procedure is that artificially low values of  $\sigma_\xi$  can be obtained when sampling regions with high spatial correlations of the magnetic field (Planck Collaboration et al. 2016a, 2016b), and these can skew the fit. While we have used a simple linear trend line to model the transition in  $\xi$ , the exact form and manner by which the transition is expected to occur are unknown. This is a significant uncertainty in the determination of  $N_{\text{H}_{2,\text{tr}}}$  and is likely several times larger than the statistical uncertainty from the fit.

Other sources of error in our estimate of  $N_{\text{H}_{2,\text{tr}}}$  are (a) the reference beam (Section 2.1), (b) the combining of data from two different telescopes, and (c) the sampling uncertainty. In Appendix, we assess the first two of these problems. We conclude that given the compounding effects of all sources of uncertainty except for (c), the total uncertainty in the value of  $N_{\text{H}_{2,\text{tr}}}$  is roughly a factor of 3. However, the uncertainties associated with (c), the incomplete sampling of L1688, are difficult to quantify. While HAWC+ observations cover only the  $\rho$  Oph A and  $\rho$  Oph E regions, our Planck analysis pertains to L1688 as a whole. In addition to  $\rho$  Oph A and  $\rho$  Oph E, L1688 also includes other dense regions (see Figure 1). We have discarded the HAWC+ data for sight lines having a column density below  $\log_{10}(N_{\text{H}_2}) = 22.3$  (see Section 3.1), but even with this restriction, the remaining HAWC+ HRO sight lines sample only  $\sim 10\%$  of the corresponding high column density sky area in L1688.



A full treatment including the other higher column density subregions of L1688 would be valuable. Maps with other polarimeters do exist for at least one target ( $\rho$  Oph C; Liu et al. 2019), but a proper HRO treatment of such maps would require consideration of uncertainties associated with reference beam contamination for instruments other than HAWC+ (see Appendix), which is beyond the scope of the present paper. In Section 5.3, we discuss the impact of the sampling certainty on our main conclusions.

Super-Alfvénic simulations from Soler et al. (2013; as discussed in Section 1) do not exhibit a transition to perpendicular alignment at any column density below  $N_{\text{H}_2} \approx 10^{22.5} \text{ cm}^{-2}$ . The estimated transition column density here is  $N_{\text{H}_2, \text{tr}} \approx 10^{21.7} \text{ cm}^{-2}$ , suggesting that L1688 is either trans- or sub-Alfvénic, as found in previous work for 11 clouds (Planck Collaboration et al. 2016b; Soler et al. 2017). Notably, one of the clouds studied in Planck Collaboration et al. (2016b) is Ophiuchus, of which L1688 is a part.

Although Soler (2019) estimated a transition column density for several regions in Ophiuchus, including L1688, their analysis is distinct from the one performed here in that it compares large-scale magnetic field and small-scale column density. Additionally, the region analyzed as L1688 in Soler (2019) is not identically defined as the region in this work. Despite these differences, when compared with the  $N_{\text{H}_2, \text{tr}} \approx 10^{21.7} \text{ cm}^{-2}$  calculated here, Soler (2019) found a similar transition column density for L1688:  $N_{\text{H}_2} \approx 10^{21.5} \text{ cm}^{-2}$  ( $N_{\text{H}_2, \text{tr}} \approx 10^{21.75} \text{ cm}^{-2}$ ).

### 5.3. Estimating the Transition Volume Density

The transition volume density at which the alignment preference shifts from parallel to perpendicular has been suggested by simulations to be tied to the physical properties of the cloud (e.g., Soler et al. 2013; Chen et al. 2016). This “critical” transition volume density ( $n_{\text{tr}}$ ) is thus a useful diagnostic. In this section, we will make an initial estimate of  $n_{\text{tr}}$  based on our HRO analysis.

Crutcher et al. (2010) reported a transition volume density at  $n_{\text{H}} \sim 300 \text{ cm}^{-3}$  ( $n_{\text{H}_2} \sim 150 \text{ cm}^{-3}$ ) for the magnetic field strength (inferred from Zeeman-splitting observations) to transition from being relatively constant ( $B \propto n^0$ ) as a function of gas density to having a power-law relationship with the gas density ( $B \propto n^{2/3}$ ). This scaling transition density is believed to correspond to the point where the magnetic field transitions from being capable of providing support against gravitational collapse to a situation where it is no longer capable of doing so. As pointed out by Chen et al. (2016; see also Soler & Hennebelle 2017; André et al. 2019), this scaling transition may correspond to the alignment transition that is revealed by the HROs. Chen et al. (2016) used Athena ideal MHD simulations to study the star-forming process in shock-compressed regions in the molecular clouds (Chen & Ostriker 2014, 2015). In this model of cloud formation, the gas is initially in a super-Alfvénic state. After the collision of the flows, a flat, dense, sub-Alfvénic postshock region is created. The snapshot when the most evolved core begins to collapse is considered. Three variants of the simulations are analyzed. Each variant was initialized with a different inflow Mach number ( $\mathcal{M} = 5, 10, \text{ and } 20$ ), but they were identical otherwise.

In a generalization of the method described in Section 3 to three dimensions, Chen et al. (2016) created synthetic 3D HROs from the simulations. 3D HROs are also discussed by

Soler et al. (2013). The alignment transition volume density is then determined as where the 3D HRO shape changes from concave to convex (i.e., the 3D HRO alignment parameter moves from  $>0$  to  $<0$ ). The scaling transition volume density from each simulation is also determined by finding the volume density at which the magnetic field strength changes from being constant as a function of volume density to becoming highly correlated with this quantity (akin to Crutcher et al. 2010). Importantly, the alignment and scaling transition volume densities introduced by Crutcher et al. (2010) are noted to roughly coincide. Chen et al. (2016) attributed this coincidence to the alignment and scaling transitions both being governed by the same physical processes.

Moving from 3D space to 2D, a similar change in HRO shape is seen in the synthetic observations when analyzing 2D projected maps. Analysis shows that this change results from the increasing importance of self-gravity, directly linking it to the transition volume density (i.e., the  $N_{\text{H}_2, \text{tr}}$  value is linked to the  $n_{\text{H}_2, \text{tr}}$  value). In short, by estimating  $N_{\text{H}_2, \text{tr}}$  observationally via the HRO method, it is possible to determine the volume density at which the gas becomes self-gravitating.

Although the transition column density values calculated for the simulated clouds in Chen et al. (2016) are not the same as the transition column density value we found in L1688, we note that these isothermal, ideal MHD simulations are scale-free, which means the column density can be rescaled (e.g., see King et al. 2018). Following the discussion and convention in King et al. (2018) and assuming  $\lambda$  is the rescaling coefficient, the physical parameters of the simulations can be rescaled as  $L \rightarrow L/\lambda$ ,  $n \rightarrow \lambda^2 n$ . This implies  $N \rightarrow \lambda N$ . Without repeating the simulations, we can therefore rescale the simulations in Chen et al. (2016) to have the same  $N_{\text{H}_2, \text{tr}}$  as the one we derived for L1688 (from Section 5.2) and use the same rescaling coefficient to calculate the corresponding rescaled  $n_{\text{H}_2, \text{tr}}$  from the original  $n_{\text{H}_2, \text{tr}}$  reported in Table 1 of Chen et al. (2016). We obtain  $\lambda$  between 0.24 and 0.60, depending on Mach number. After rescaling, the resulting  $n_{\text{H}_2, \text{tr}}$  values range between  $10^{3.8}$  and  $10^{4.2} \text{ cm}^{-3}$ .

Deriving  $n_{\text{H}_2, \text{tr}}$  from  $N_{\text{H}_2, \text{tr}}$  can be seen as a division by an effective length. When using the simulations from Chen et al. (2016) to obtain  $n_{\text{H}_2, \text{tr}}$ , this effective length is several times smaller than the plane-of-sky dimensions of L1688. This is consistent with the results of numerous simulation works finding that flattened slablike structures are typical (e.g., Inoue & Inutsuka 2016; Li & Klein 2019).

The  $n_{\text{H}_2, \text{tr}}$  values we find here can be compared to an estimate of the same quantity for a different molecular cloud made by Fissel et al. (2019). Using molecular line density tracers, Fissel et al. (2019) estimated the transition volume density value of Vela C to be  $\sim 10^3 \text{ cm}^{-3}$ , with uncertainties on the level of 1 order of magnitude. Their method combined polarization maps from the BLASTPol balloon-borne polarimeter and intensity maps of various molecular lines from Mopra to estimate the projected Rayleigh statistic (PRS), a statistic analogous to  $\xi$ . By then quantifying the characteristic densities corresponding to each molecular species, the point where the PRS transitions from parallel alignment to no preferred orientation or a weakly perpendicular alignment was estimated to determine the alignment transition volume density. Given the factor of 10 uncertainty of Fissel et al. (2019) and our own sampling uncertainties, which are difficult to quantify, we

conclude that there is no significant tension between our result and that of Fissel et al. (2019).

The difference between the values we obtain here using the simulations as the framework ( $10^{3.8}$ – $10^{4.2}$   $\text{cm}^{-3}$ ) and the values obtained in Crutcher et al. (2010;  $\sim 150 \text{ cm}^{-3}$ ) is approximately a factor of  $\sim 100$ . The factor of 3 uncertainty in  $N_{\text{H}_2}$  discussed in Section 5.2 propagates to approximately an order of magnitude uncertainty in  $n_{\text{H}_2}$  here. However, there remains the sampling uncertainty, which is difficult to quantify. Specifically, it is unknown whether analysis of the unsampled subregions of L1688 would result in generally negative  $\xi$  values as found for  $\rho$  Oph A and  $\rho$  Oph E. Should the unsampled regions of L1688 present different HRO behaviors, the resulting transition density could change significantly. Recalculation of  $N_{\text{H}_2, \text{tr}}$  for  $\rho$  Oph A and  $\rho$  Oph E separately show a variation of, at most, a factor of a few ( $\sim 2.5$ ). Analysis of the remaining unsampled regions will be required to constrain this variation further. Nonetheless, based on the subregions sampled so far, it would appear that there may be a large ( $\times 100$ ) discrepancy between  $\sim 150 \text{ cm}^{-3}$ , the value of Crutcher et al. (2010), and  $\sim 10^4 \text{ cm}^{-3}$ , determined here.

Recent work reexamining and extending the Bayesian models from Crutcher et al. (2010) obtained significantly higher scaling transition volume density values. Specifically, Jiang et al. (2020) found a transition volume density value of  $n_{\text{H}_2} \sim 560 \text{ cm}^{-3}$ , lessening the discrepancy. As more Zeeman-splitting observations become available (i.e., Thompson et al. 2019), it is likely that this value will be updated further.

## 6. Conclusions

In this paper, we have used  $154 \mu\text{m}$  polarization observations from HAWC+ and Herschel-derived column density maps to characterize the alignment between the magnetic field and elongated column density structures of  $\rho$  Oph A and  $\rho$  Oph E using the HRO method. Using this method, we found a preference for perpendicular alignment at higher densities. This preference is observed for each region analyzed individually, as well as when analyzed together.

Combining a Planck HRO analysis of L1688 completed at lower densities and this HAWC+ result allows an HRO analysis over scales of  $\sim 0.02$ – $3.1$  pc ( $33''6$ – $1^\circ 3$  at  $d \approx 137$  pc). Using the combined data set, we estimated the transition column density at which the L1688 region of Ophiuchus changes from parallel to perpendicular alignment to be  $N_{\text{H}_2, \text{tr}} \approx 10^{21.7} \text{ cm}^{-2}$ . This is consistent with the results of Planck Collaboration et al. (2016b).

To explore the implications of our results, we calculate a value for the alignment transition volume density under the assumption that the ideal MHD colliding flow models of Chen et al. (2016) apply to L1688. We conclude that our value of  $N_{\text{H}_2, \text{tr}}$  implies  $n_{\text{H}_2, \text{tr}} \approx 10^4 \text{ cm}^{-3}$ .

In the model of Chen et al. (2016), the alignment transition volume density approximately equals the scaling transition volume density, which has been previously measured by Crutcher et al. (2010) for an ensemble of clouds. However, the latter is observed by Crutcher et al. (2010) to be approximately 2 orders of magnitude smaller than the values we find for the alignment transition volume density in L1688.

The reexamination of Zeeman observations by Jiang et al. (2020) presents one possible path to help reconcile these values. The discrepancy might be further ameliorated if a complete sampling of the high-density sight lines of L1688

changes the result of the combined Planck/HAWC+ HRO analysis. The two separate regions we observed with HAWC+ ( $\rho$  Oph A and  $\rho$  Oph E) give similar results but together represent only 10% of all high-density sight lines in L1688. Further observations of this cloud using HAWC+/SOFIA will be valuable. Finally, it seems likely that crucial insights can be gained by using a variety of simulations to carry out the conversion of  $N_{\text{H}_2, \text{tr}}$  to  $n_{\text{H}_2, \text{tr}}$  and comparing the results.

We thank the anonymous referee for extensive feedback and helpful suggestions. This work is based on observations made with the NASA/DLR Stratospheric Observatory for Infrared Astronomy (SOFIA). SOFIA is jointly operated by the Universities Space Research Association, Inc. (USRA), under NASA contract NAS2-97001, and the Deutsches SOFIA Institut (DSI) under DLR contract 50 OK 0901 to the University of Stuttgart. Financial support for this work was provided by NASA through award Nos. SOF 06-0116 and SOF 07-0147 issued by USRA to Northwestern University. This research has made use of data from the Herschel Gould Belt survey (HGBS) project (<http://gouldbelt-herschel.cea.fr>). The HGBS is a Herschel Key Programme jointly carried out by the SPIRE Specialist Astronomy Group 3 (SAG 3), scientists of several institutes in the PACS Consortium (CEA Saclay, INAF-IFSI Rome and INAF-Arcetri, KU Leuven, MPIA Heidelberg), and scientists of the Herschel Science Center (HSC). This work makes use of observations obtained with Planck (<http://www.esa.int/Planck>), an ESA science mission with instruments and contributions directly funded by ESA Member States, NASA, and Canada. W.K. was supported by the New Faculty Startup Fund from Seoul National University. C.Y.C. acknowledges support by NSF AST-1815784. Z.Y.L. is supported in part by NASA 80NSS20K0533.

*Facility:* SOFIA (HAWC+).

*Software:* numpy (Harris et al. 2020), scipy (Virtanen et al. 2020), matplotlib (Hunter 2007), astropy (Astropy Collaboration et al. 2013), aplpy (Robitaille & Bressert 2012).

## Appendix A

### Uncertainties in the Transition Column and Volume Densities

As described in Section 2, we rejected sky pixels for which the polarization measurements were considered too contaminated by the reference beam flux to be of use. However, it is possible that even small levels of contamination may affect our analysis, as variations may alter the value of the HRO parameter by modifying the relative orientation angle. To estimate the magnitude of this effect, we follow the procedure described in Novak et al. (1997) and Chuss et al. (2019). Assuming an unknown polarization angle but a uniform polarization fraction of 10% in the reference beam, we can compute  $\Delta \hat{E}_{\text{ref}}$ :

$$\Delta \hat{E}_{\text{ref}} = \frac{1}{2} \arctan \left[ \frac{p_r w}{(p_m^2 - p_r^2 w^2)^{\frac{1}{2}}} \right]. \quad (\text{A1})$$

This value represents the largest polarization angle “error” possible due to reference beam contamination. (See Section 2 for symbol definitions.) After calculating  $\Delta \hat{E}_{\text{ref}}$ , we then modify all of our measured polarization angles with this maximum “error” to produce two extreme cases. One case is



produced by increasing the nominal  $\hat{E}$  value for all sky positions by  $\Delta\hat{E}_{\text{ref}}$ ; the other is produced by decreasing  $\hat{E}$  by  $\Delta\hat{E}_{\text{ref}}$ . After reapplying the procedures from Section 3 using these modified scenario polarization angles, we find that the resulting  $N_{\text{H}_{2,\text{tr}}}$  value changes by less than a factor of  $\sim 1.25$ .

As the uncertainty in the polarization angle measurement is not directly encapsulated in the HROs and the subsequent linear regression to obtain  $N_{\text{H}_{2,\text{tr}}}$ , we now consider this source of uncertainty. In terms of its effect on the analysis, this uncertainty will play a similar role to that of the reference beam contamination. In that case, the median  $\Delta\hat{E}_{\text{ref}}$  “error” value is computed to be  $\approx 19^\circ$ . By comparison, the median uncertainty in the polarization angle for data used in this study is only  $\approx 1^\circ$ . As a result, we expect that any effect of the uncertainty in the polarization angle measurement will be subdominant to that of the reference beam contamination and thus minimally affect the resulting  $N_{\text{H}_{2,\text{tr}}}$  value.




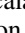





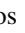
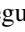


The existence of reference beam contamination also presents an issue when merging polarimetric observations from different instruments, as we do here (e.g., Figure 1). Owing to differences in referencing strategies and methods, the role of the reference beam can vary greatly depending on the instrument. As noted above, reference beam contamination can alter the observed polarization angle, which can severely impact the HRO results. Thus, a thorough investigation is required prior to any combined analysis. As the Planck instrument does not employ referencing methods in its observations, the Planck data do not suffer from this type of contamination.

However, other complications may arise from conducting a combined analysis of Planck and HAWC+ polarimetry. The angular resolutions of these two data sets differ; the Planck data have an FWHM resolution of  $5'$ , and our HAWC+ data are at  $36''$ . As a result of their lower resolution, the Planck observations are unable to resolve any small-scale field disorders that may exist. A more disordered field would suggest less preferential alignment and thus a flatter HRO. The corresponding  $\xi$  would potentially be closer to zero than nominally suggested by the Planck analysis. However, at the large scales and lower column densities investigated by Planck, the field is believed to be sub-Alfvénic (Planck Collaboration et al. 2016b). The field is thus likely well ordered, suggesting that this effect is likely minimal.

An additional source of uncertainty is introduced by the relatively short observing wavelength of the HAWC+ polarimetry. At  $154\ \mu\text{m}$ , the magnetic field traced by HAWC+ may not follow the column density structure mapped by Herschel at submillimeter wavelengths nor be directly comparable to the  $850\ \mu\text{m}$  (353 GHz) observations of Planck. It is possible that the shorter-wavelength observations used here are less sensitive to the colder dust. Certainly, polarimetric observations at longer wavelengths would be beneficial. However, comparisons suggest that the variations between the measured magnetic field orientation at these wavelengths are typically not significant. Observations of OMC-1 at 53, 89, 154, and  $214\ \mu\text{m}$  using HAWC+ and  $850\ \mu\text{m}$  using POL-2 show general agreement in magnetic field orientation despite the wavelength difference (Pattle et al. 2017; Chuss et al. 2019). This is also true when comparing the  $850\ \mu\text{m}$  POL-2 observations of  $\rho$  Oph A from Kwon et al. (2018) with the  $154\ \mu\text{m}$  observations presented in Santos et al. (2019; and here).

As stated in Section 5.2, we estimate the total uncertainty resulting from the effects discussed here to be a factor of 3 on our value of  $N_{\text{H}_{2,\text{tr}}}$ . However, these effects are subdominant compared to the sampling uncertainty (also described in Section 5.2).

## ORCID iDs

Dennis Lee  <https://orcid.org/0000-0002-3455-1826>  
 Che-Yu Chen  <https://orcid.org/0000-0002-9209-7916>  
 Erin G. Cox  <https://orcid.org/0000-0002-5216-8062>  
 Frankie J. Encalada  <https://orcid.org/0000-0002-3566-6270>  
 Rachel Harrison  <https://orcid.org/0000-0003-2118-4999>  
 Woojin Kwon  <https://orcid.org/0000-0003-4022-4132>  
 Di Li  <https://orcid.org/0000-0003-3010-7661>  
 Zhi-Yun Li  <https://orcid.org/0000-0002-7402-6487>  
 Leslie W. Looney  <https://orcid.org/0000-0002-4540-6587>  
 Giles Novak  <https://orcid.org/0000-0003-1288-2656>  
 Fabio P. Santos  <https://orcid.org/0000-0002-9650-3619>  
 Dominique Segura-Cox  <https://orcid.org/0000-0003-3172-6763>  
 Ian Stephens  <https://orcid.org/0000-0003-3017-4418>

## References

- Andersson, B. G., Lazarian, A., & Vaillancourt, J. E. 2015, *ARA&A*, **53**, 501  
 André, P., Di Francesco, J., Ward-Thompson, D., et al. 2014, in *Protostars and Planets VI*, ed. H. Beuther et al. (Tucson, AZ: Univ. Arizona Press), 27  
 André, P., Hughes, A., Guillet, V., et al. 2019, *PASA*, **36**, e029  
 André, P., Men'shchikov, A., Bontemps, S., et al. 2010, *A&A*, **518**, L102  
 Andre, P., Montmerle, T., Feigelson, E. D., Stine, P. C., & Klein, K.-L. 1988, *ApJ*, **335**, 940  
 Astropy Collaboration, Robitaille, T. P., Tollerud, E. J., et al. 2013, *A&A*, **558**, A33  
 Chapman, N. L., Davidson, J. A., Goldsmith, P. F., et al. 2013, *ApJ*, **770**, 151  
 Chen, C.-Y., King, P. K., & Li, Z.-Y. 2016, *ApJ*, **829**, 84  
 Chen, C.-Y., & Ostriker, E. C. 2014, *ApJ*, **785**, 69  
 Chen, C.-Y., & Ostriker, E. C. 2015, *ApJ*, **810**, 126  
 Chuss, D. T., Andersson, B. G., Bally, J., et al. 2019, *ApJ*, **872**, 187  
 Crutcher, R. M., Wandelt, B., Heiles, C., Falgarone, E., & Troland, T. H. 2010, *ApJ*, **725**, 466  
 Davidson, J. A., Novak, G., Matthews, T. G., et al. 2011, *ApJ*, **732**, 97  
 Doi, Y., Hasegawa, T., Furuya, R. S., et al. 2020, *ApJ*, **899**, 28  
 Enoch, M. L., Evans, N. J. I., Sargent, A. I., & Glenn, J. 2009, *ApJ*, **692**, 973  
 Fissel, L. M., Ade, P. A. R., Angilè, F. E., et al. 2016, *ApJ*, **824**, 134  
 Fissel, L. M., Ade, P. A. R., Angilè, F. E., et al. 2019, *ApJ*, **878**, 110  
 Hamaguchi, K., Corcoran, M. F., & Imanishi, K. 2003, *PASJ*, **55**, 981  
 Harper, D. A., Runyan, M. C., Dowell, C. D., et al. 2018, *JAL*, **7**, 1840008  
 Harris, C. R., Millman, K. J., van der Walt, S. J., et al. 2020, *Natur*, **585**, 357  
 Hildebrand, R. H., Davidson, J. A., Dotson, J. L., et al. 2000, *PASP*, **112**, 1215  
 Hull, C. L. H., Mocz, P., Burkhart, B., et al. 2017, *ApJL*, **842**, L9  
 Hunter, J. D. 2007, *CSE*, **9**, 90  
 Inoue, T., & Inutsuka, S.-i. 2016, *ApJ*, **833**, 10  
 Jiang, H., Li, H.-b., & Fan, X. 2020, *ApJ*, **890**, 153  
 King, P. K., Fissel, L. M., Chen, C.-Y., & Li, Z.-Y. 2018, *MNRAS*, **474**, 5122  
 Körtgen, B., & Soler, J. D. 2020, *MNRAS*, **499**, 4785  
 Kwon, J., Doi, Y., Tamura, M., et al. 2018, *ApJ*, **859**, 4  
 Ladjelate, B., André, P., Könyves, V., et al. 2020, *A&A*, **638**, A74  
 Li, H.-b., Fang, M., Henning, T., & Kainulainen, J. 2013, *MNRAS*, **436**, 3707  
 Li, P. S., & Klein, R. I. 2019, *MNRAS*, **485**, 4509  
 Li, Z. Y., Banerjee, R., Pudritz, R. E., et al. 2014, in *Protostars and Planets VI*, ed. H. Beuther et al. (Tucson, AZ: Univ. Arizona Press), 173  
 Liu, J., Qiu, K., Berry, D., et al. 2019, *ApJ*, **877**, 43  
 Liu, T., Li, P. S., Juvela, M., et al. 2018, *ApJ*, **859**, 151  
 Matthews, T. G., Ade, P. A. R., Angilè, F. E., et al. 2014, *ApJ*, **784**, 116  
 McKee, C. F., & Ostriker, E. C. 2007, *ARA&A*, **45**, 565  
 Motte, F., Andre, P., & Neri, R. 1998, *A&A*, **336**, 150  
 Novak, G., Dotson, J. L., Dowell, C. D., et al. 1997, *ApJ*, **487**, 320  
 Palmeirim, P., André, P., Kirk, J., et al. 2013, *A&A*, **550**, A38  
 Pattle, K., Lai, S.-P., Di Francesco, J., et al. 2021, *ApJ*, **907**, 88  
 Pattle, K., Ward-Thompson, D., Berry, D., et al. 2017, *ApJ*, **846**, 122  
 Pillai, T. G. S., Clemens, D. P., Reissl, S., et al. 2020, *NatAs*, **4**, 1195

- Planck Collaboration, Ade, P. A. R., Aghanim, N., et al. 2015, [A&A](#), [576](#), [A104](#)
- Planck Collaboration, Adam, R., Ade, P. A. R., et al. 2016a, [A&A](#), [586](#), [A135](#)
- Planck Collaboration, Ade, P. A. R., Aghanim, N., et al. 2016b, [A&A](#), [586](#), [A138](#)
- Planck Collaboration, Aghanim, N., Akrami, y., et al. 2020, [A&A](#), [641](#), [A1](#)
- Poglitsch, A., Waelkens, C., Geis, N., et al. 2010, [A&A](#), [518](#), [L2](#)
- Robitaille, T., & Bressert, E. 2012, APLpy: Astronomical Plotting Library in Python, Astrophysics Source Code Library, ascl:[1208.017](#)
- Sadavoy, S. I., Stephens, I. W., Myers, P. C., et al. 2019, [ApJS](#), [245](#), [2](#)
- Santos, F. P., Chuss, D. T., Dowell, C. D., et al. 2019, [ApJ](#), [882](#), [113](#)
- Seifried, D., Walch, S., Weis, M., et al. 2020, [MNRAS](#), [497](#), [4196](#)
- Soam, A., Liu, T., Andersson, B. G., et al. 2019, [ApJ](#), [883](#), [95](#)
- Soler, J. D. 2019, [A&A](#), [629](#), [A96](#)
- Soler, J. D., Ade, P. A. R., Angilè, F. E., et al. 2017, [A&A](#), [603](#), [A64](#)
- Soler, J. D., & Hennebelle, P. 2017, [A&A](#), [607](#), [A2](#)
- Soler, J. D., Hennebelle, P., Martin, P. G., et al. 2013, [ApJ](#), [774](#), [128](#)
- Sugitani, K., Nakamura, F., Watanabe, M., et al. 2011, [ApJ](#), [734](#), [63](#)
- Tassis, K., Dowell, C. D., Hildebrand, R. H., Kirby, L., & Vaillancourt, J. E. 2009, [MNRAS](#), [399](#), [1681](#)
- Thompson, K. L., Troland, T. H., & Heiles, C. 2019, [ApJ](#), [884](#), [49](#)
- Virtanen, P., Gommers, R., Oliphant, T. E., et al. 2020, [NatMe](#), [17](#), [261](#)
- Ward-Thompson, D., Pattle, K., Bastien, P., et al. 2017, [ApJ](#), [842](#), [66](#)
- Wilking, B. A., Gagné, M., & Allen, L. E. 2008, in Handbook of Star Forming Regions, Volume II: The Southern Sky, Vol. 5, ed. B. Reipurth (San Francisco, CA: ASP), [351](#)
- Zucker, C., Speagle, J. S., Schlafly, E. F., et al. 2019, [ApJ](#), [879](#), [125](#)